Physics of the Earth and Planetary Interiors 172 (2009) 183–198

Contents lists available at ScienceDirect

Physics of the Earth and Planetary Interiors

journal homepage: www.elsevier.com/locate/pepi

Variable seismic structure near the 660 km discontinuity associated with stagnant slabs and geochemical implications

Fumiko Tajima*, Ikuo Katayama, Tsuyoshi Nakagawa

Department of Earth and Planetary Systems Science, Graduate School of Science, Hiroshima University, Higashi Hiroshima 739-8526, Japan

ARTICLE INFO

Article history:
Received 13 March 2008
Received in revised form 5 September 2008
Accepted 8 September 2008

Keywords:
Stagnant slab
Broadband seismic waveform modeling
Variable discontinuity depths
Geochemical implications

ABSTRACT

This study reports a compilation of reflectivity synthetic modeling for the structure of the upper mantle transition zone with high velocity anomalies (HVA's), associated with the northwestern Pacific subduction zones. Here, the employed method of reflectivity synthetics effectively determines the structure of flattened HVA, i.e. stagnant slab, as triplicated regional body waves are very sensitive to the velocity discontinuities in the transition zone. Results show a distribution of HVA's with or without a depression of the "660 km" discontinuity depth, which indicates a possible variation of geochemical properties at the bottom of the upper mantle. A hypothesis is proposed for this implication, i.e. that the structural variation may represent the contrast between a hydrous garnet-rich layer (subducted crust) and bulk peridotite associated with a stagnant slab, which is supported by the results of recent laboratory experiments. The garnet-rich layer can flow and descend faster than bulk peridotite as hydrous garnet is weaker and denser than peridotite in the transition zone. Given that the Clapeyron slope for hydrous garnet–perovskite is positive at ~660 km, two zones of HVA with, and without a depression in the discontinuity depth may exist next to each other at the bottom of the transition zone. This variation of the discontinuity depths coincides with the segmentation identified at deeper depths (>629 km) in a P-wave travel-time tomography model although the resolution of the tomography inversion is limited to elaborate the discontinuity structure.

1. Introduction

The fate of subducted slabs has long been a focus in mantle dynamics. Mineral physicists predicted possible presence of stagnating slabs, or megaliths in the mantle transition zone (MTZ) associated with phase transformation of the cold slab above the discontinuity depth at ~660 km (Ringwood, 1967; Ringwood and Irifune, 1988), where ringwoodite (the gamma-Mg_2Sio_4 high-pressure phase of olivine) transforms to a denser phase assemblage (perovskite + magnesiowüstite), but this phase change may be delayed and occur at depths below 660 km due to the negative Clapeyron slope of this phase transition. In these circumstances, the subducted cold slab may deform and form a megalith at the base of the MTZ (Ringwood and Irifune, 1988; Ringwood, 1994). In the MTZ, majorite–garnet is the primary mineral phase of subducted oceanic crust (mid-ocean ridge basalt, MORB) and may persist to depths of 660–690 km, corresponding to the range where the density of model pyrolite crosses MORB, becoming 100–200 kg/m^3 denser (Irifune and Ringwood, 1993). Buoyancy of the upper MORB layer may promote separation from the denser peridotite beneath, leading to a growth of slab megalith at the base of the MTZ. The importance of the role of the subducted crust layer is clear. However, recent results of seismological and experimental studies suggest that a correction in this scenario is necessary. This correction arises largely from seismic observations on the variation of the "660 km" phase transformation depth, and new findings of mantle rheology and phase transformation characteristics in water-rich environments.

2. Seismic observation of stagnant slab

2.1. Long-wavelength features

In the early 1990s, seismic tomography models (van der Hilst et al., 1991; Fukao et al., 1992) presented three-dimensional (3D) images of the velocity structure of the mantle, in which variable high-velocity anomalies (HVA) were detected in subduction regimes. The stunning images of the large bulk of flattened HVA in the MTZ, denoted the "stagnant slab", stimulated debate about whether subducting slabs penetrate into the lower mantle or not.

Since then a number of seismic tomography models show long-wavelength HVA structures which are interpreted to be stagnant

* Corresponding author. Tel.: +81 82 424 7463; fax: +81 82 424 0735.
E-mail address: fumiko-tajima@hiroshima-u.ac.jp (F. Tajima).

0031-9201/$ – see front matter © 2008 Elsevier B.V. All rights reserved.
doi:10.1016/j.pepi.2008.09.013

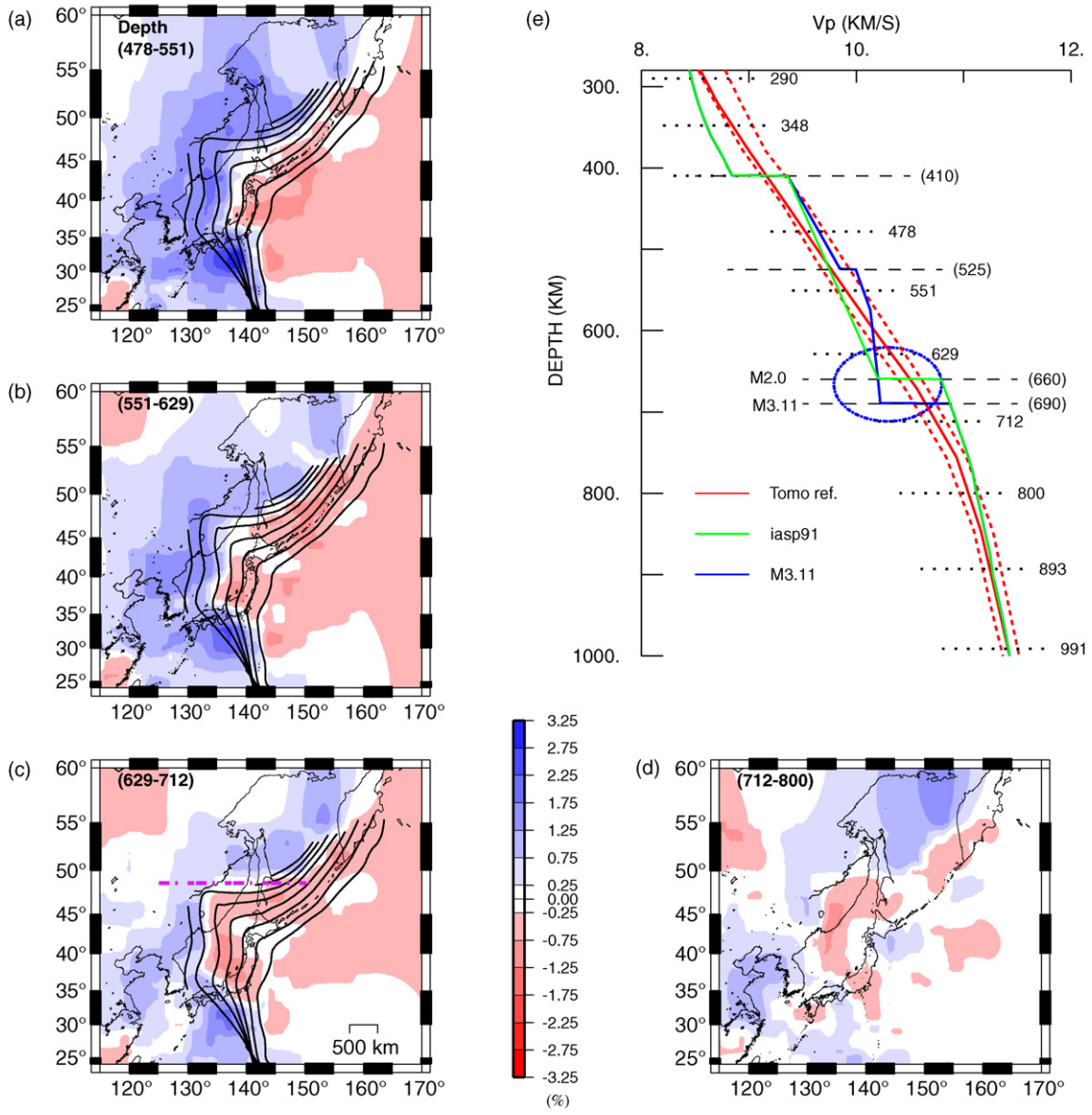

Fig. 1. Images of stagnant slab (HVA, navy) captured in the tomography model of Fukao et al. (2001) in the northwestern Pacific in the depth range: (a) 478–551 km, (b) 551–629 km, (c) 629–712 km, and (d) 712–800 km. The equi-depth contours of the subduction zone are drawn from 0 to 600 or 700 km with an interval of 100 km. Note the segmentation boundary of the HVA coincides the equi-depth contours at >629 km (dashed pink line in (c)). (e) layered seismic velocity models to represent stagnant slab structure in relation to a standard model iasp91 (green): M3.11 (navy) that has HVA in the deeper part of the transition zone and depression of the discontinuity depth to 690 km, M.2.0 that has HVA similar to M3.11 but without depression of the discontinuity depth, and the tomography reference model (red solid line) with dotted lines for its perturbation. The horizontal dotted lines show the depths (such as 478, 551, 629, 712, 800 km) where the boundaries of the blocks are set in the tomography model.

slabs above the 660 km discontinuity in the northwestern Pacific [see Fig. 1 after the model of Fukao et al. (2001)], penetration of the HVA into the lower mantle before stagnation in the uppermost lower mantle in the Java subduction zone, or even an extended HVA zone to the bottom of the lower mantle (Fukao et al., 2001; Grand et al., 1997; Widiyantoro and van der Hilst, 1996; van der Hilst et al., 1997; Grand, 2002). The lateral extent of an HVA that is shallower than 551 km (Fig. 1a) is a broad, continuous region beneath Sakhalin, the northeastern Eurasian plate and the Philippine Sea plate. However, the HVA region appears to be segmented at depths below 629 km, i.e. the HVA image beneath southeastern China is separated from the HVA zone beneath Sakhalin to the west (Fig. 1c and d).

The early generation tomography models, which were derived using primary P-wave travel-time data from the International Seismological Centre seismicity catalog, had limitations in resolving structure in the MTZ (Tajima and Grand, 1995, 1998). The modeling algorithms of long wavelength tomography analyses do not necessarily have resolving ability of the structure near the phase transformation depth (see Inoue et al., 1990). The reference model of Fukao et al. (1992, 2001) has a structure with a smooth increase in velocity with depth, in which no discontinuities were included (see Fig. 1e). The 660 km seismic discontinuity depth, which is critically important for slab dynamics, was included in the blocks set in the depth range between 629 and 712 km in the tomography inversion. Thus, while tomography techniques are robust for capturing images of anomalies, they are limited for resolving the detailed structure associated with the mantle fabric distribution located at the bottom of the MTZ. There is still a substantial variation between the models in terms of their shorter wavelength features (Grand, 2002).

2.2. Broadband waveform modeling and velocity models M3.11 and M2.0

On the other hand, seismic body waves recorded at regional distances show waveforms of triplicated arrivals due to the velocity discontinuities at ~410 and 660 km and provide a strong sampling of the MTZ as they turn in that depth range. Tajima and Grand (1995, 1998) determined layered models for the subhorizontal HVA region using a reflectivity method (Fuchs and Müller, 1971). Here, the reflectivity synthetic modeling is effective to determine a layered structure incorporating the secondary arrivals of triplicated broadband waveforms that are highly sensitive to the structure around the turning depths near the discontinuity. Models M2.0 and M3.11 thus derived delineate the MTZ structure with stagnant slab (Fig. 1e; see also Tajima and Nakagawa, 2006).

Model M3.11 is characterized by HVA of up to +3% relative to a standard model, iasp91 of Kennett and Engdahl (1991) in the deeper part of the MTZ (~525–660 km) above the discontinuity, and the discontinuity is depressed to 690 km. The HVA in the depth range between ~525 and 660 km may represent the flattened cold slab, and the depression of the discontinuity depth is consistent with the prediction by mineral physics studies in context with the negative Clapeyron slope of ringwoodite to perovskite and magnesiowüstite transformation (Ringwood and Irifune, 1988).

Model M2.0 represents the structure that has HVA in the deeper part of the MTZ like M3.11 but is not accompanied by broad depression of the 660 km discontinuity depth. Whether the discontinuity depth is depressed (M3.11) or not (M2.0), affects little the velocity at the phase transition depth, i.e. velocity is almost constant in the range between 660 and 690 km. Note that this depth range is included in the blocks set between 629 and 712 km in the tomography model of Fukao et al. (2001) (see the comparison between the layered models and the tomography reference model in Fig. 1e).

The sensitivity of the triplicated waveforms is demonstrated in the examples of seismic data, which strongly sampled the HVA zone in the MTZ and were recorded at the Chinese Digital Seismic Network station HIA for three deep focus events A5, A6 and A2 in the Kurile subduction zone (Fig. 2; see Fig. 3 for the locations). The observed P waveforms (top bold traces) are compared with the corresponding synthetic waveforms (thin traces) calculated using an optimum model (M3.11 or M2.0), and the other models including iasp91 (Fig. 2a). Note that the seismic rays of these events sampled the structure closely to each other in the region where a broad HVA was captured in the tomography model (see Fig. 1) but the optimum structural model is different from each other.

Fig. 2b shows the triplicated seismic rays from these events to HIA. The sampling and bottoming (or turning) depths of multiple arriving waves vary depending on the source depth and station distance (i.e. showing whether the rays turn in the MTZ or in the uppermost lower mantle). Fig. 2c shows the diagrams of reduced P-wave travel-times as a function of distance that were calculated with models M3.11, M2.0 and iasp91 for each of these events. The range of triplication, and the time interval between the first and secondary arrivals, vary depending on the structure whether or not it is accompanied by the HVA in the MTZ and a depression of the 660 km discontinuity, and the source depth. In other words the time intervals between the first and later arrivals of triplicated regional body waves are very sensitive to the structure around the discontinuity depth.

Using a reflectivity modeling of triplicated broadband waveform data, Tajima and Grand (1998) and Tajima et al. (1998) pointed out structural variation in the MTZ zone in the northwestern Pacific where tomography models (e.g. van der Hilst et al., 1991; Fukao et al., 1992) determined a large scale flattened HVA or a stagnant slab.

2.3. Variable discontinuity depths at ~660 km

Recently we evaluated the tomographic images of HVA (Fukao et al., 2001) using an improved data set of broadband waveforms from about 50 selected deep focus events ($H \geq 300$ km) and several mid-depth events ($100 < H < 300$ km) that occurred during the period 1990–2007 (see the event information in Tables 1 and 2). The results confirmed the details of the structural variation in the tomographic HVA regions associated with the Kurile, Japan, and Izu–Bonin subduction zones with additional insight for the flattened HVAs that have a normal discontinuity depth (e.g. 660 km).

Fig. 3 shows the individual rays with structural distinction for events from the Kurile and Izu-Bonin subduction zones along which the structures are distinguished among the models: (a) M3.11 by the solid navy line, (b) M2.0 or M2.0+ by the dotted or dashed navy line, and (c) others by the black line. Here, the M2.0+ data (dashed navy line) indicates a model that could be either the M2.0 or M3.11 model, and the term "others" includes all waveforms that could not be modeled using a layered structure. In Appendix A the observed waveform data are compared with synthetics calculated using an optimum model and other layered models (Fig. A1).

The sensitivity of the triplicated waves is best to the structure near the turning depth. The small ellipses in different colors indicate the approximate bottoming locations where the rays reach the bottom and turn upwards in the HVA region with a discontinuity depression (navy), or without a discontinuity depression (light blue). The grey ellipses indicate the bottoming locations of the rays for "other". Here note that the ellipses are illustrated just to show the bottoming locations with the widths which are much larger than the estimated Fresnel zones there. Fig. 4 is the summary of the structure along these seismic rays.

Many of the body waves, which strongly sampled the regions of HVA, can be modeled using the M3.11 model, the M2.0 model, or a model with slight modifications to these. The HVA zones beneath the equi-depth lines ≥500 km from Sakhalin to the west are delineated by the M3.11 model well (see the rays from events A5, A4, A12, and A16 to the HIA) and bounded by the structure of the M2.0 model (rays from A6 and Am2 to the HIA, and from A3, A7, A8, A11, and A15 to the BJT) or the M2.0+ model (from A12, A13, and A14 to the BJT). Some waveforms that propagate in the vicinity of these ray paths could not be modeled using a layered structure (rays shown with black lines and small gray ellipses in Fig. 3c). The structure along the rays may have strong heterogeneity of relatively short wavelength such as a very localized low velocity anomaly near the deep events resulting in interference of layered modeling. The anomalous broadened P wave at HIA recorded for A2 was reported as being possible converted SV to P waves in a localized low-velocity anomaly (LVA) zone in the stagnant slab while no such anomaly was observed in the corresponding SH waves and P waves at other stations (Tajima and Nakagawa, 2006).

Likewise, the central part of the HVA zone from the Izu-Bonin subduction zone to the northwest is delineated by the M3.11 data (rays from B19 and B20 to the MDJ, from B16, B18, and B28 to the HIA, and from B2, B7, B14, B21, and B28 to the BJT), and is bounded by the structure of the M2.0 data on the northern side (A7 and A8 to SSE, B6 and B7 to HIA). There were also some waveform data that propagated in the vicinity of the HVA zone but could not be modeled using a layered model as mentioned above. The MTZ structure beneath the southwestern Japan that is modeled with M2.0 may have the situation suggested by Niu et al. (2005) (see the discussion in Section 3.3).

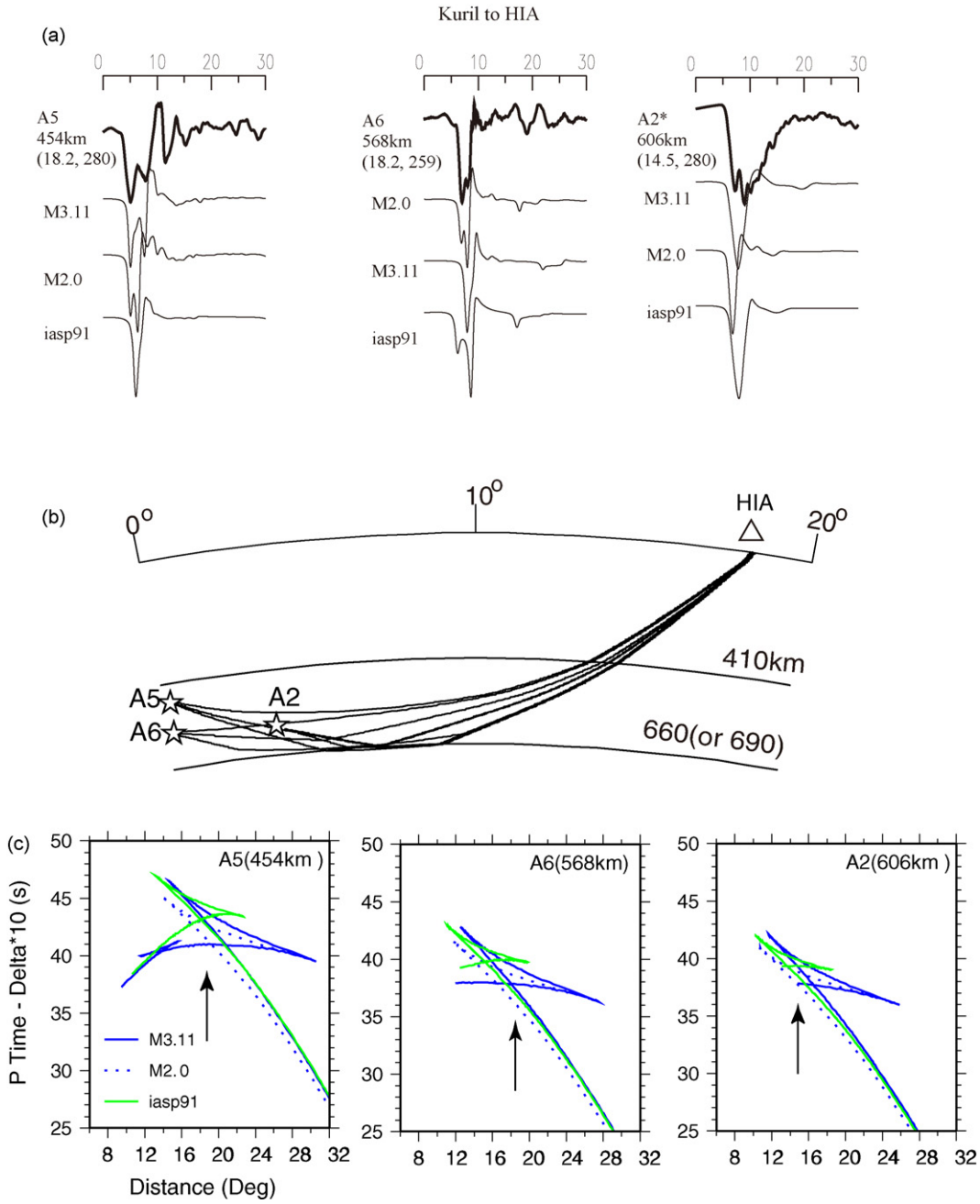

Fig. 2. Example of triplicated waveforms and sensitivity of triplicated travel-time arrivals to the different structures: (a) waveform data for 30 s (bold traces) recorded at Chinese station HIA for deep focus events (A5, A6, and A2) in the Kurile subduction zone (see the locations in Fig. 3) in comparison with synthetics (thin traces) calculated using model M3.11, M2.0 and a standard model iasp91. (b) Triplicated seismic rays from these events to illustrate the structure of strong sampling. Each of the triplicated rays either bottoms in the transition zone, reflects at the discontinuity, or bottoms below the transition zone. (c) Reduced P-wave travel time diagrams for these events calculated with models M3.11, M2.0 and iasp91 to illustrate the sensitivity of triplicated travel-times to the structural variation near the discontinuity depth. The arrows indicate the station distances for events A5, A6 and A2, respectively. The time intervals of multiple arrivals are very sensitive to the velocity structure as well as the source depths that characterize the waveforms.

In general, the regions represented by the M3.11 data adjoin the zones of the M2.0 data. The preferred model for the structure beyond the subduction front in the Kuriles is M2.0 (see rays from Am1 and Am4, and perhaps Am3 to the HIA). However, we admit that the ray sampling of the region is sparse due to the limited distribution of seismicity and adequate stations. It is also interesting to note that the boundaries between different structures approximately coincide with the segmentation boundaries identified (as little or no anomalies sometimes) at deeper depths in the tomography model (>629 km, Fig. 1c and d).

3. Interpretation for geochemical properties

3.1. Implication of variable discontinuity depths

Model M3.11 is suitable to delineate the structure of a flattened slab (stagnant slab) which consists primarily of ringwoodite. The structural change from the M3.11 to M2.0 data takes place via a steep gradient in space. Taking the profile for the assemblage of ringwoodite, the lack of a depression in the 660 km discontinuity may be interpreted using the tem-

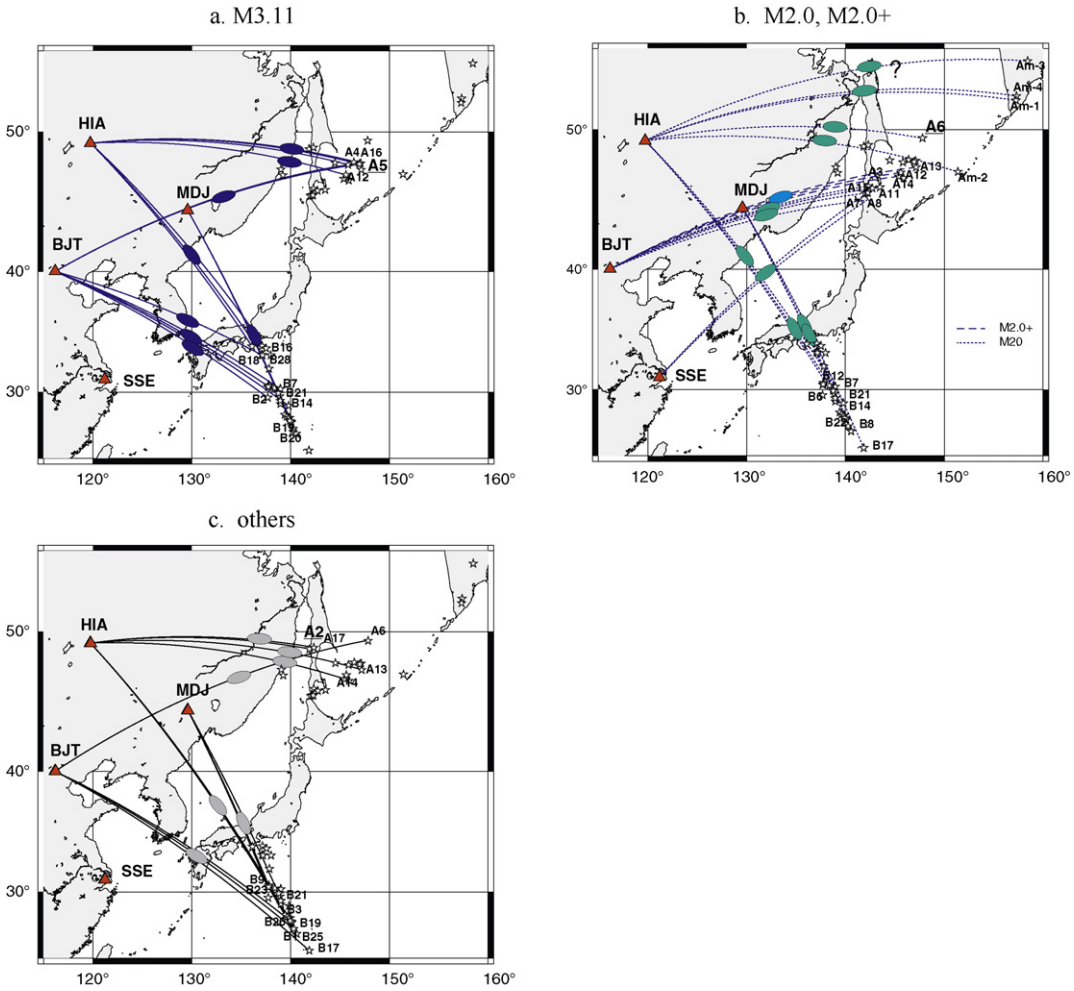

Fig. 3. Seismic rays with structural distinction for events (shown with stars; see Tables 1 and 2) from the Kurile and Izu-Bonin subduction zones to stations HIA, BJT, MDJ or SSE along which the structures are inferred from the waveform modeling in terms of (a) M3.11, (b) M2.0 or M2.0+, and (c) others. The event ID's of A5, A6 and A2 are slightly enlarged and underlined in (a), (b) and (c), respectively. The small ellipses in different colors show the bottoming locations with (navy) or without (light blue) depression of the 660 km discontinuity. The gray ellipses show the bottoming areas of seismic rays for which layered models do not explain the observed waveforms sufficiently.

Table 1
List of deep focus events in the Kurile subduction zone.

Event ID	Date	Time (UT)	Lat (°N)	Lon (°E)	Dep (km)	Mag	(ϕ, δ, λ)
A1	1990/04/21	22:56:54.22	47.49	139.02	490.4	mb 5.5	46, 68, 160
A2**	1990/05/12	04:50:09.00	48.89	141.86	606.0	mb 6.3	172, 29, −151
A3**	1990/08/20	00:03:52.80	46.17	142.31	309.0	mb 5.7	170, 61, 29
A4**	1991/07/05	10:58:28.50	47.82	145.82	465.0	mb 5.5	316, 35, −5
A5**	1992/03/27	20:28:14.80	47.92	147.10	454.0	mb 5.5	23, 40, 122
A6**	1992/05/22	16:19:53.70	49.44	147.81	568.0	mb 5.6	159, 47, 126
A7**	1992/06/16	05:51:03.70	45.70	142.26	317.0	mb 5.7	43, 58, 173
A8*	1993/01/24	21:30:51.08	45.71	142.17	306.6	5.7	63, 38, −147
A9	1994/04/28	18:30:02.70	45.66	142.00	304.4	mb 5.5	None
A10	1995/02/18	13:29:05.35	46.73	145.88	335.3	mb 5.6	59, 39, 149
A11*	1995/03/10	05:22:21.28	46.08	143.50	336.7	5.8	66, 64, −177
A12*	1997/11/28	06:10:47.49	47.11	145.60	390.6	mb 5.6	255, 14, −73
A13*	1999/02/05	14:37:51.62	47.48	147.15	391.0	Mw 5.8	253, 27, −17
A14*	2000/07/10	09:58:18.67	46.85	145.38	352.7	Mw 5.8	290, 36, −24
A15*	2002/02/09	16:56:07.77	46.02	142.72	344.2	Mw 5.5	49, 35, 146
A16*	2002/03/07	00:07:06.41	47.85	146.96	433.6	Mw 5.6	1, 9, 57
A17*	2002/11/05	08:47:26.62	48.98	142.30	604.9	Mw 5.6	314, 52, 6
A18	2002/11/17	04:53:47.65	47.99	146.40	456.4	mb 5.8	316, 9, 30
A19	2003/07/27	06:25:31.76	47.10	139.21	467.5	Mw 6.7	61, 44, 158
A20b	2004/11/07	02:02:26.17	47.95	144.48	474.0	Mw 6.1	231, 60, 154
Am-1*	2002/10/16	10:12:23.42	51.87	157.26	123.3	Mw 6.2	101, 18, 163
Am-2*	2004/07/08	10:30:47.13	47.16	151.37	123.0	Mw 6.3	127, 33, −161
Am-3*	2006/05/22	13:08:02.95	54.27	158.45	197.0	Mw 6.2	262, 19. −51
Am-4*	2007/05/30	20:22:12.60	52.14	157.31	116.0	mb 6.4	110, 11, 180

*, ** results are shown; ** see also (Tajima and Grand, 1995, 1998); Events with an ID of Am-no. occurred at mid-depths ($100 < H < 300$ km).

Table 2
List of deep focus events in the Izu-Bonin subduction zone.

Event ID	Date	Time (UT)	Lat (°N)	Lon (°E)	Dep (km)	Mag	(ϕ, δ, λ)
B1*	1990/04/14	08:00:14.41	27.28	140.06	464.1	mb 5.6	13, 47, −31
B2*	1990/08/05	01:34:57.84	29.51	137.70	521.7	mb 5.9	28, 52, −177
B3**	1992/01/20	13:37:03.00	27.98	139.40	499.0	mb 5.8	47, 40, −157
B4	1992/06/29	16:04:12.66	27.80	139.60	532.1	mb 5.8	52, 47, −146
B5*	1992/08/29	19:19:05.50	33.19	137.97	289.0	mb 5.9	75, 14, 159
B6**	1992/10/30	02:49:48.10	29.24	138.97	370.0	mb 5.8	43, 40, −150
B7*	1993/07/05	15:20:57.71	30.27	138.94	418.0	mb 5.5	92, 45, −140
B8*	1993/07/20	13:26:04.49	27.37	140.06	464.2	mb 5.6	133, 47, −138
B9*	1993/10/04	06:39:16.11	30.60	137.77	479.8	mb 5.5	45, 54, −138
B10*	1993/10/11	15:54:21.20	32.05	137.80	347.0	mb 6.0	93, 9, −179
B11*	1995/07/07	21:15:19.70	33.97	137.12	333.0	mb 5.8	328, 15, 75
B12**	1995/07/29	16:18:44.80	30.35	138.38	436.0	mb 5.5	73, 19, 175
B13	1996/03/16	22:04:06.72	28.97	138.98	481.5	mb 5.9	68, 213, −163
B14*	1996/05/19	21:19:08.61	28.79	139.80	412.2	mb 5.6	140, 20, −120
B15	1996/06/26	03:22:05.31	27.70	139.88	491.3	mb 5.5	110, 25, −135
B16*	1996/10/18	16:44:48.50	33.78	137.51	341.0	mb 5.7	11, 14, 94
B17*	1998/02/07	01:13:39.13	24.74	141.84	552.3	mb 5.7	128, 31, −122
B18*	1998/06/01	07:35:51.00	33.93	136.10	403.1	mb 5.6	329, 12, 63
B19*	1999/01/12	02:32:28.90	26.73	140.25	476.0	Mw 5.9	10, 51, −27
B20*	1999/07/03	05:30:11.91	26.30	140.56	449.5	Mw 6.1	15, 44, −43
B21*	1999/12/05	22:00:32.54	29.89	138.76	432.0	Mw 5.7	85, 41, −178
B22*	2000/01/10	16:40:44.45	27.32	140.04	476.3	Mw 5.7	155, 47, −127
B23*	2000/06/09	22:35:15.30	30.43	137.70	490.8	Mw 5.8	286, 53, −37
B24	2000/06/09	23:31:46.03	30.45	137.75	494.0	Mw 6.2	245, 36, −77
B25*	2000/10/27	04:21:53.95	26.26	140.56	412.3	Mw 6.1	142, 24, 148
B26*	2002/06/03	09:15:02.04	27.45	139.91	506.9	Mw 5.8	100, 22, −137
B27	2003/11/12	08:26:43.95	33.24	137.05	381.8	Mw 6.3	50, 34, 156
B28b*	2005/02/22	11:20:25.28	33.18	137.15	369.5	Mw 5.6	54, 25, 141
B29b	2005/04/19	01:46:56.95	29.64	138.89	425.8	Mw 5.9	69, 31, −166

See the notations in Table 1.

perature which is normal beneath the flattened slab (Tajima and Grand, 1998). However, the observed structural change is more rapid than that expected from the temperature gradient associated with a cold slab. Instead, we postulate a variable distribution of geochemical properties at the bottom of the upper mantle where the contrast of a hydrous garnet-rich layer (subducted crust of MORB origin) versus bulk peridotite is involved. Two recent experiments under high-pressure and

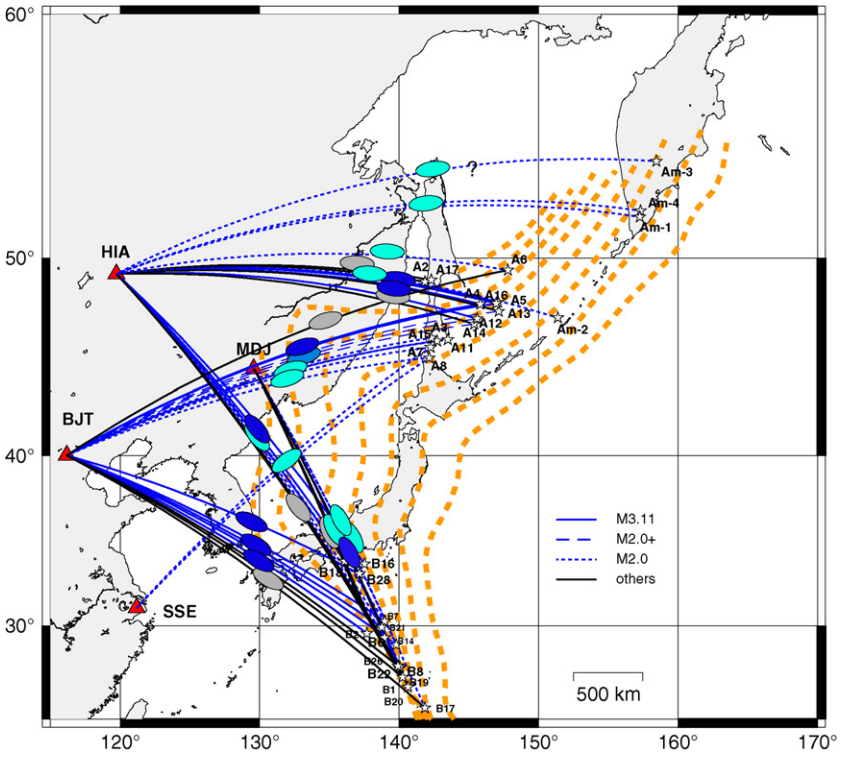

Fig. 4. Summary of the structural variation in terms of M3.11, M2.0 or M2.0+, and others (see the caption of Fig. 1 for the equi-depth contours).

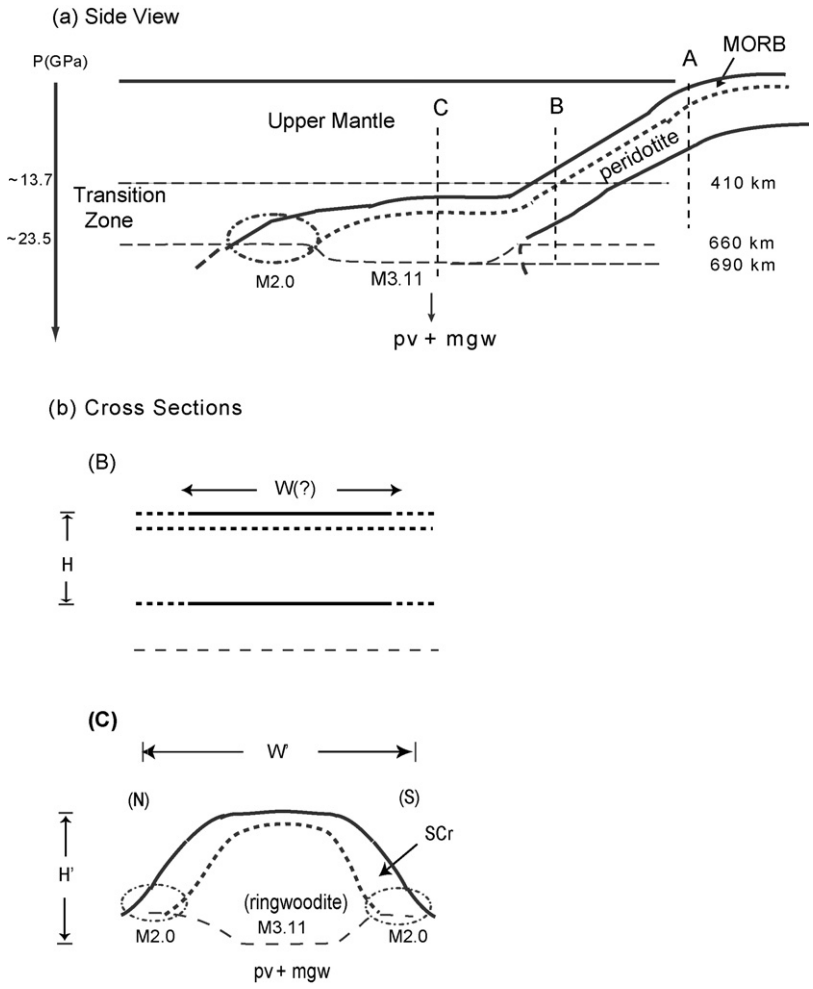

Fig. 5. Schematic illustration of stagnant slab: (a) side view. The phase transformation depth near 660 km is depressed in the center of the stagnant slab and the depression gradually disappears toward the boundary of the stagnant slab; (b) cross-sections along B and C in (a). The lateral boundaries of HVA at the bottom of the transition zone (indicated by W′) are recognized in the segmented tomography images as well as from the waveform modeling. Scr, pv, and mgw denote subducted crust, perovskite and magnesiowüstite, respectively. The lateral extent of HVA at shallower depths (illustrated as W along B) is broad and continuous from the Kuriles to the Izu-Bonin subduction zone in the tomography images (see Fig. 1a).

high-temperature conditions provide supportive feedback for this hypothesis.

3.2. Supporting results from experiments

Sano et al. (2006) showed that the Clapeyron slope of garnet to perovskite in hydrous MORB at ~660 km is positive, and suggest that there may be no depression of the phase transformation depth if the temperature associated with the slab is lower than 1200 °C. Under these conditions, the M2.0 model may delineate a structure that consists primarily of hydrous garnet (subducted crust of MORB origin) at the bottom of the upper mantle. Then the next question is, "why and how does the garnet-rich zone of the subducted crust exist next to the zone of ringwoodite that is modeled with the M3.11 model?"

A more recent experiment provides new evidence for a weaker strength garnet-rich layer than the olivine dominant mantle under water-rich conditions (Katayama and Karato, 2008) while dry garnet is considered to be harder than olivine (Karato et al., 1995). In this case, the hydrous garnet-rich subducted crust can flow and descend over the bulk peridotite in the MTZ as MORB has a higher density than that of pyrolite in the MTZ (Irifune and Ringwood, 1993). Here, note that the rheology experiments were carried out at a relatively low-pressure (P = 2 GPa), and a large extrapolation is needed when these results are applied to the conditions existing near the 660 km discontinuity. Nonetheless, a systematic study on garnet with various compositions and analog materials has shown that garnet follows the homologous temperature scaling law (Karato et al., 1995). Accordingly, this scaling predicts that the conditions where garnet is weaker than mantle phases (wadsleyite and ringwoodite are likely harder than olivine (Xu et al., 2005)) are still within the possible range of water content in the MTZ (C_{OH} ~1000 ppm H/Si).

3.3. Schematic model

Fig. 5 gives a schematic model: (a) a side view of the subducting slab, and (b) a cross-section along B and C in (a), which show the slab at a shallower depth and at the bottom of the MTZ, respectively. The lateral extent (W) of the subducting plate is broad, and no segmentation is observed at shallower depths (cross-section A to B, also see Fig. 1a). The subducting slab flattens as it enters the MTZ, and bulk high-pressure phase of peridotite (ringwoodite) accumulates over the depressed phase boundary (modeled using M3.11).

The subducted crust, i.e. the garnet-rich layer that is denser and weaker than peridotite, may flow over and descend faster than the

bulk peridotite. Accordingly, an M2.0 zone is formed beyond the front and at the sides of the flattened slab in the MTZ. This may result in a segmentation of the plate and also cause a reduction in strength and deformation of the subducted slab. The tomography images show a segmentation in the distribution of the HVA in the deeper MTZ (>629 km in Fig. 1c and d), which may suggest the boundaries of the subducted slab (illustrated by W′ for cross-section C in Fig. 5b), as well as the structural boundaries recognized in the waveform modeling (Figs. 3 and 4).

However, some of the regions that were modeled with the M2.0 model may have the situation of a subducting slab as illustrated along profile B in Fig. 5a, i.e. the subducted cold slab enters the MTZ but has not reached the phase transformation depth. A receiver function analysis determined such situation existed in the seismic velocity structure for the MTZ beneath the Philippine Sea plate (Niu et al., 2005). The distribution of the possible hydrous garnet rich layer at the bottom of the MTZ is yet to be explored as the seismic sampling of the region is still too sparse to refine it.

4. Discussion and summary

We reiterate that the seismic rays of the regional waves bottom in and sample strongly the MTZ, and the relative time intervals between the first and later arrivals in triplicated waveforms are very sensitive to the structure near the discontinuity. Thus, we effectively determined the variation of the discontinuity depth associated with the flattened part of the subducted slab (stagnant slab) using an improved data set of regional broadband waveforms.

4.1. Velocity models and measured properties

The mantle composition properties estimated by seismic studies, which are not unambiguous, can be checked for various conditions and validated through synthetic high pressure and temperature experiments. However, there have been only limited velocity measurements on majorite (the high-pressure phase of garnet) in laboratory experiments (e.g. Sinogeikin and Bass, 2002; Kono et al., 2007; Irifune et al., 2008). A study on the seismic velocity of the garnet-rich layer in the MTZ (Shen and Blum, 2003) has discussed garnet having a lower seismic velocity than the surrounding mantle (pyrolite) (Ita and Stixrude, 1992), but its exsolution to Ca-perovskite at depths deeper than 600 km (Irifune and Ringwood, 1987) may increase the velocity (Duffy and Anderson, 1989), and the inclusion of stishovite (about 10 vol%) in MORB (Li et al., 1996) may also contribute to an increase of velocity.

Recently, Kono et al. (2007) show that the garnetite with a MORB composition has significantly lower P- and S-wave velocities than wadsleyite and ringwoodite with a composition of $(Mg_{0.9},Fe_{0.1})_2SiO_4$ under the pressure conditions of the MTZ. However, the ultrasonic P- and S-wave velocity measurements of dry materials were performed at pressures up to 14.3 GPa at room temperature, and then the estimates of elastic properties for the MTZ condition has been made with a large extrapolation. They also pointed out that the MORB majorite has very different bulk and shear moduli from those of the Mg end-member garnets and suggest possible misleading interpretations for seismic wave speed structures should they adopt elastic properties of simple end-members under the MTZ conditions.

Irifune et al. (2008) carried out combined *in situ* X-ray and ultrasonic measurements under the pressure and temperature conditions of the MTZ and showed that majorite exhibits substantially lower velocities relative to wadsleyite and ringwoodite. However, they also suggested the possibility of progressive formation of $CaSiO_3$-rich perovskite (which has high velocities) from the majorite phase leaving possible support for the increase of the seismic velocities at the bottom of the MTZ (Irifune et al., 2008). The experimental technology has advanced in recent years, but the control of experimenting *in situ* high pressure and temperature conditions in the MTZ is still limited having substantial uncertainties in the estimated elastic properties. Thus, the subducted crust (hydrous majorite) accumulated at the bottom of the MTZ that is represented by the M2.0 model is plausible given the present state of rheological knowledge.

The structure that could not be modeled using a layered model in the vicinity of the M3.11 or M2.0, like the one which was sampled by the waveform recorded at HIA from event A2, may be a very localized anomalous narrow zone with fluid or melt produced from dehydration of hydrous slab materials (Tajima and Nakagawa, 2006). A recent study of seismic waveform modeling using a 3D finite difference method provides supportive results for the existence of a highly localized or very narrow LVA due to melts or fluids (Nakagawa and Tajima, submitted for publication). This study showed that the broadened P waveform was produced as the results of SV to P conversion at the LVA zone. However, the LVA zone has very little effects on the travel times of P or SH waves since it is very narrow. The phase relationship of peridotite–2 wt% water to a pressure of 30 GPa is complicated due to the lateral temperature gradient with the cold-slab geotherm (Ohtani et al., 2004), which may result in a distribution of very localized anomalous zones.

4.2. Tomography image of stagnant slab

As was pointed out for the tomographic models, first arriving P waves used in the inversion of ISC travel-time data do not necessarily sample the MTZ structure strongly, and have very little resolution for the structure around the 660 km discontinuity depth. The smooth structure as a function of depth of the reference model also limits the resolution of the structure in the depth range between 629 and 712 km. Nonetheless, Nakagawa and Tajima (submitted for publication) confirmed the stable but blurred image of stagnant slabs in the tomography model of Fukao et al. (2001) although the actual size of a stagnant slab should be smaller than the image. They applied the tomography perturbation to a 2D or 3D model constructed from iasp91 with or without a lowered discontinuity depth to 690 km and computed synthetic waveforms using a finite difference method. The synthetic waveforms are very close to the waveforms which are modeled either with M3.11 or M2.0.

Published models suggest that the Pacific plate has subducted at the Kurile to Japan trenches since 84 Ma continuously while the formation of the Philippine Sea plate ~50 Ma was followed by an eastward trench retreat ~30–17 Ma and westward advance of a lesser extent since 17 Ma (Seno and Maruyama, 1984). For the southern Kurile subduction zone the volume of subducted slab in the past 17 My is estimated by the thickness of slab ~80 km times 10 cm/year times 17 My (Tajima and Grand, 1998; Tajima et al., 1998). This volume is roughly equivalent to the volume of a stagnant slab estimated from model M3.11, i.e. the thickness of 170 km times the extent of less than 1000 km.

The result suggests that the stagnant slab either moves somewhere else out of the MTZ, or descends further into the lower mantle. The tomography image in the deeper transition zone (>629 km) indicates segmentation of the subducted plate which had a broad extent at shallower depths (see Fig. 1a, b, and c). The characteristics of variable geochemical properties may have caused the plate segmentation that affects the slab dynamics.

4.3. Variable geochemical properties and relative flow speed

Based on the rapid change of the discontinuity depth, we postulated a variable distribution of geochemical properties at the bottom of the upper mantle, i.e. a hydrous garnet-rich layer (subducted crust of MORB origin) is represented by model M2.0 and bulk peridotite by M3.11.

We roughly estimate the relative flow speed of a hydrous garnet-rich layer over bulk peridotite by adopting a simple model of a one-dimensional channel flow on an inclined plane (see Problem 6-4 in Turcotte and Schubert, 2002). The velocity profile u in the channel is given by

$$u = \frac{\rho \cdot g \cdot \sin\ \alpha}{2\mu}(h^2 - y^2) \quad (1)$$

where h is the thickness of the flow (originally crust), y is the coordinate measured perpendicular to the inclined plane ($y = h$ is the surface of the plane), α is the inclination of the plane to the horizontal, μ is the viscosity, and g is the gravity acceleration. The average speed of the flow is given by

$$\tilde{u} = \frac{\rho \cdot g \cdot h^2 \cdot \sin\ \alpha}{3\mu} \quad (2)$$

Replace ρ in (2) with the density contrast of MORB versus pyrolite which is 200 kg/m^3 (Irifune and Ringwood, 1993) as our concern is to estimate just the relative flow speed. If a value of h = 7.00E + 3 m (7 km) is used for the crustal thickness, and g = 9.8 m/s^2, μ = 1.00E + 19 Pa s, and $\alpha = 45^\circ$ are used for the gravity constant, viscosity, and the angle of inclination in (2), the average flow speed $\tilde{u}$ is calculated to be 2.26E–09 m/s or about +7.0 cm/year (relative to the plate subduction). This order of the relative flow speed is comparable to the speed of mantle convection and suitable to assume the accumulation of the subducted crust next to the bulk peridotite over the discontinuity.

4.4. Summary

This study attempted to reduce the gap between long-wavelength seismic tomography and mineral physics studies, primarily using a broadband waveform analysis of triplicated regional body waves. Results elaborate the structure near the discontinuity depths, effectively supplement the resolution data from tomography modeling, and provide additional insight into the properties associated with stagnant slabs. Numerical modeling may be helpful to synthesize the slab dynamics accounting for variable distribution of geochemical properties associated with stagnant slabs (Tajima et al., 2005).

Acknowledgements

We thank Yoshio Fukao and Masayuki Obayashi for providing us with the tomography model data and useful discussion. We appreciate George Helffrich and two anonymous reviewers for the insightful review comments that helped improve the clarity of the manuscript. The figures were produced using GMT (Wessel and Smith, 1995). This research was supported by Grants-in-Aid for Scientific Research no. 16340130 from the Japan Society for the Promotion of Science (JSPS), and no. 17037004 and no. 19013002 from the Ministry of Education, Culture, Sports, Science and Technology (MEXT) of Japan.

Appendix A

The observed waveform data (bold traces on top) are compared with the synthetics (thin traces) calculated using a reflectivity method and the layered models (Fig. A1). Here, the waveforms with a good S/N are selected for comparison (see the list of events in Tables 1 and 2). The observed waveform data are retrieved for a time window of 30 s that starts 5 s prior to the theoretical arrival time calculated with iasp91. The time intervals of triplicated arrivals are tested for an optimum model. Groups a, b and c correspond to the groups in Fig. 3, i.e. the optimum structural model for group a is M3.11, that for group b M2.0, and that for group c is others.

The synthetic waveforms calculated with an optimum model (second traces from the top) are in good agreement with the observed waves and distinguished from those calculated using other models. The time intervals between the first and later arrivals are very sensitive to the velocity structure around the turning depths along the rays as well as the source depths and propagation distances (see Fig. 2). On the other hand the calculated first arrival times using the layered structures do not necessarily fit the observed ones. The reflectivity synthetic modeling with a layered structure is often limited to fully model the waveforms which propagated through the 3D structure in the subduction zone.

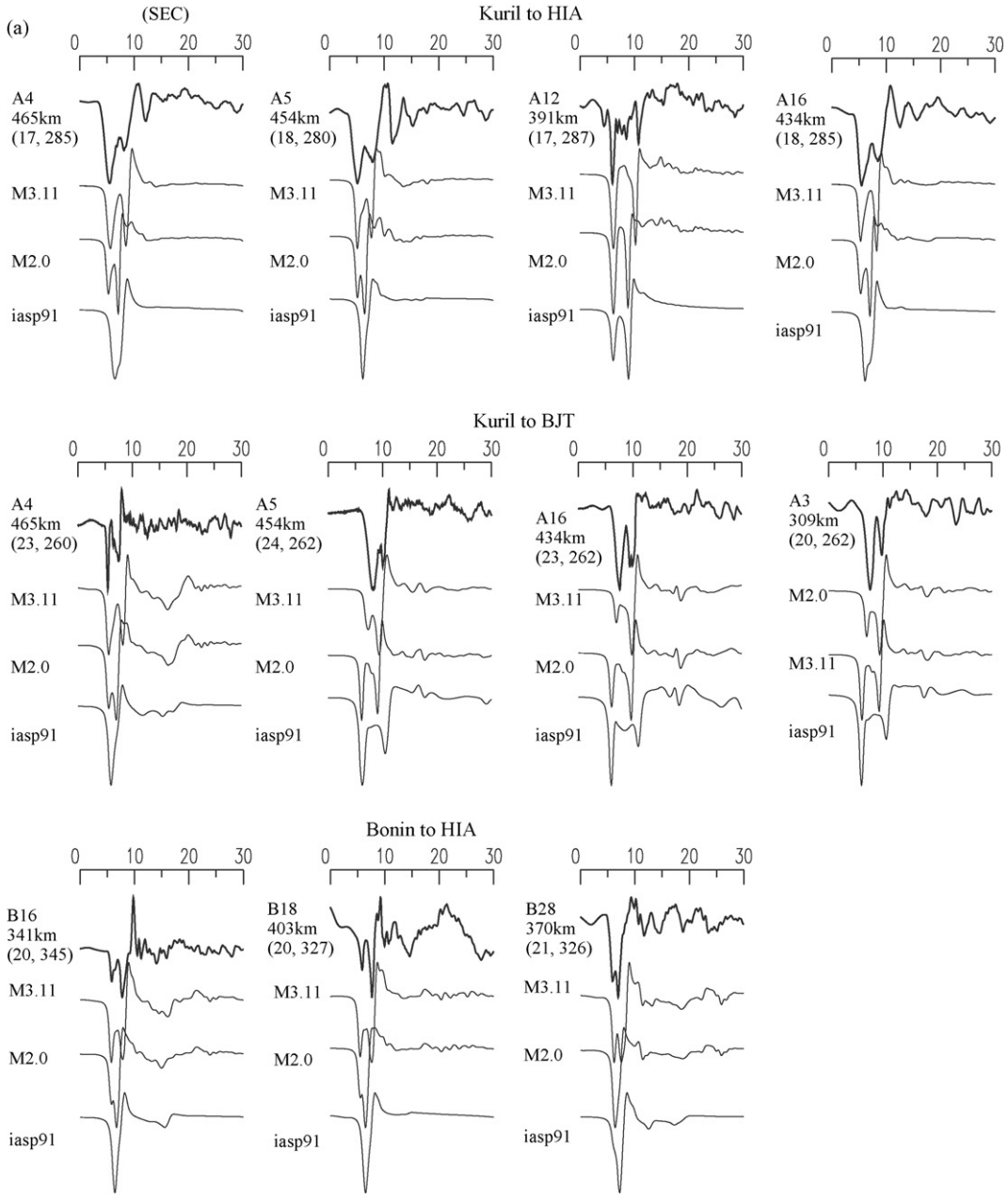

Fig. A1. Observed waveform data (bold traces on top) in comparison with synthetics calculated using different models (thin traces) in groups (a) M3.11, (b) M2.0 or M2.0+, and (c) others that correspond to the groups (a), (b) and (c) shown in Fig. 3. The source depth, station distance (deg) and azimuth (deg) are labeled below each of the event ID's.

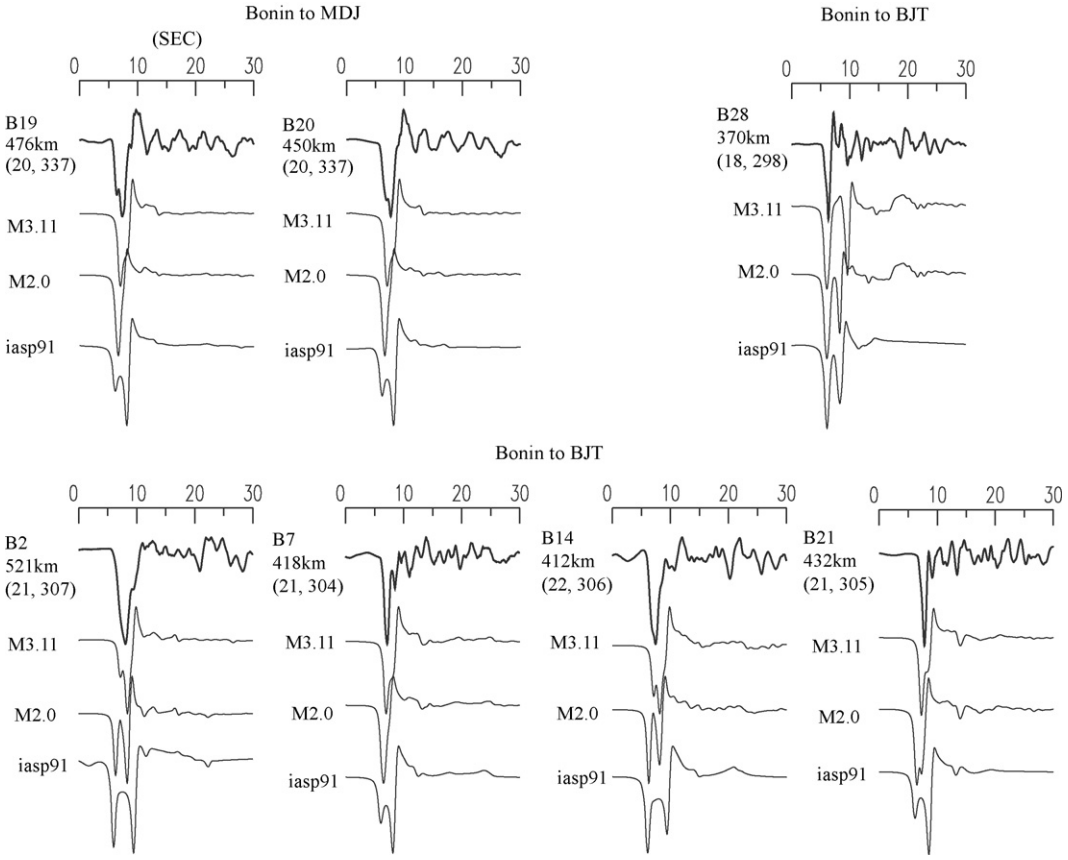

Fig. A1. (*Continued*)

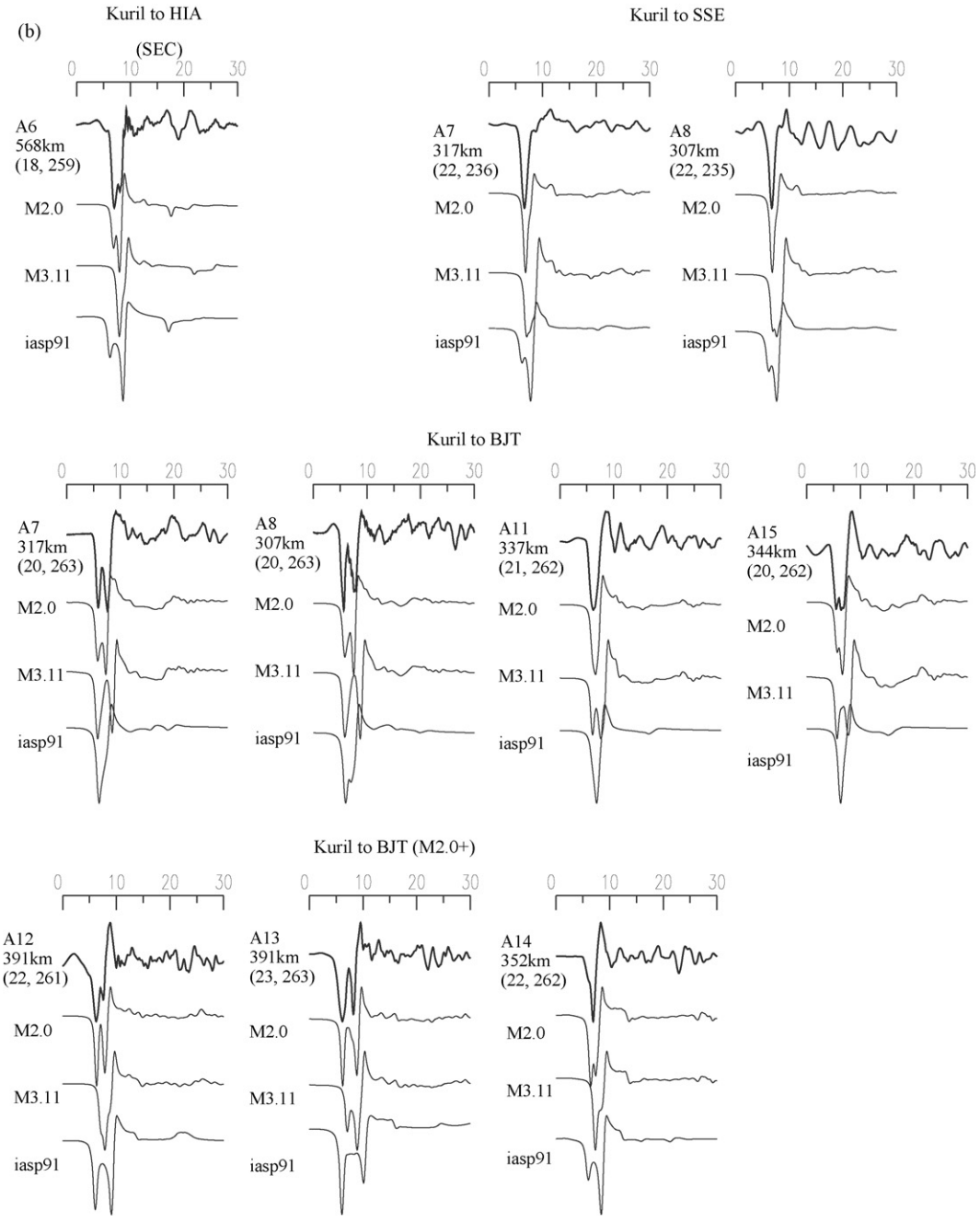

Fig. A1. (*Continued*)

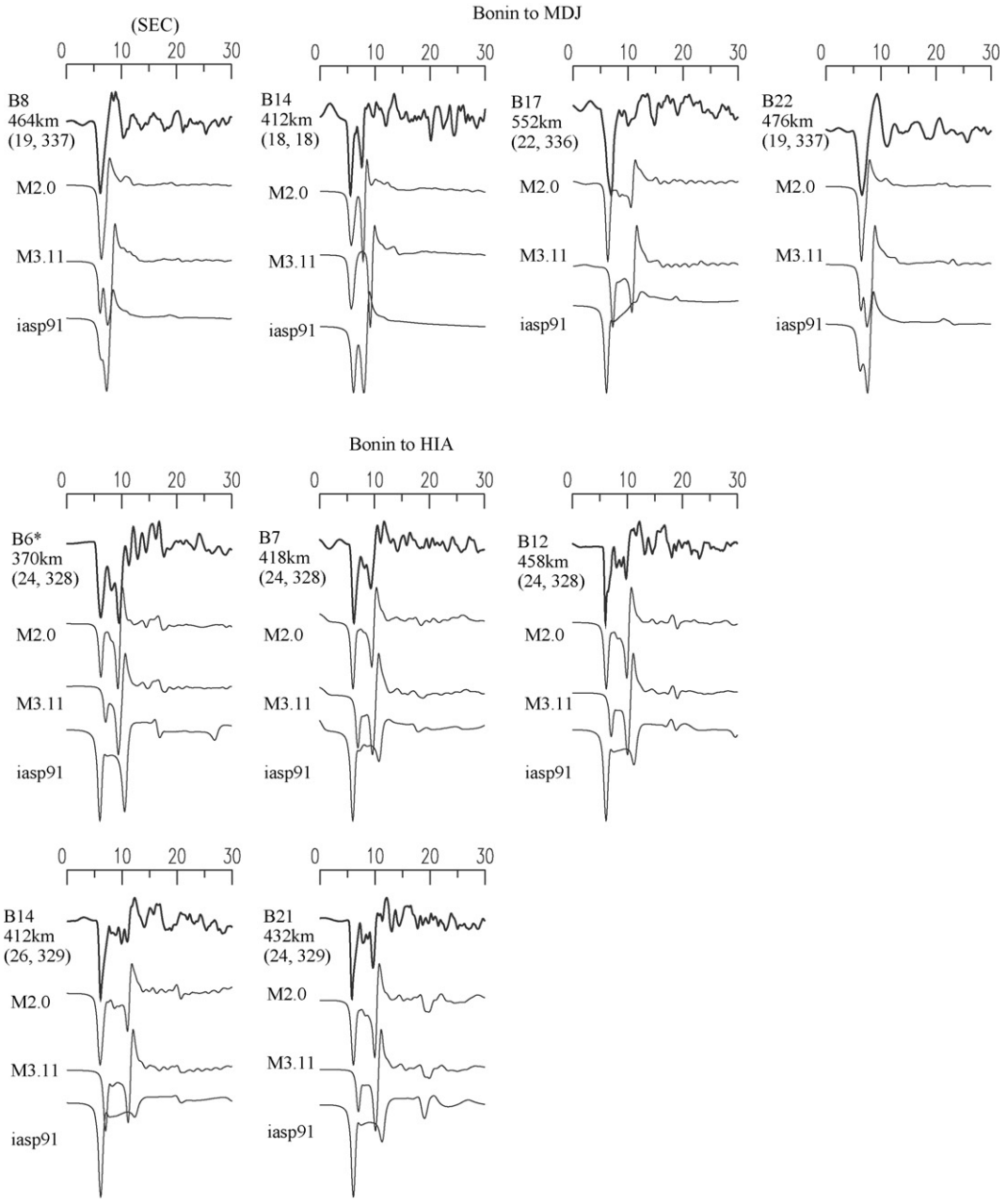

Fig. A1. (*Continued*)

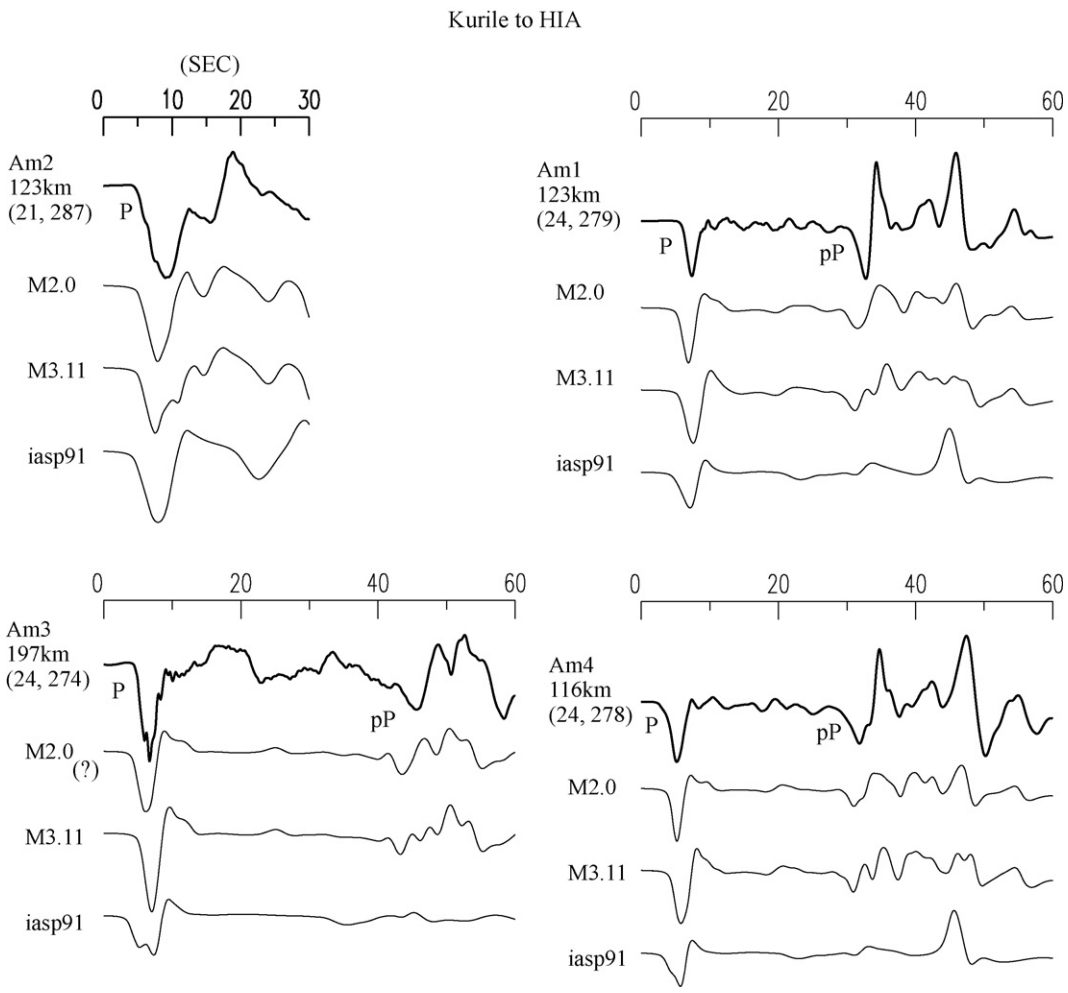

Fig. A1. (*Continued*)

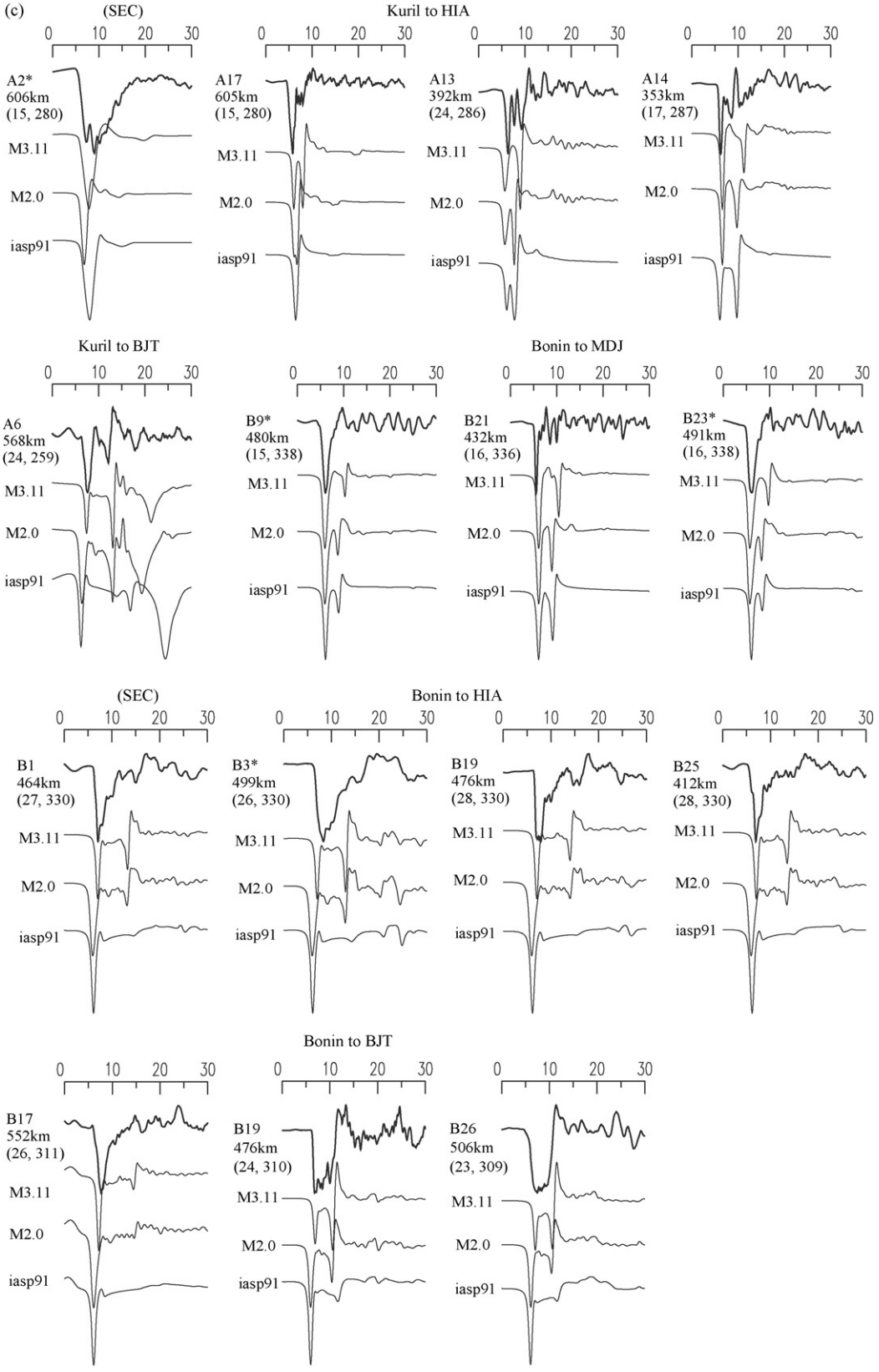

Fig. A1. (*Continued*).

References

Duffy, T.S., Anderson, D.L., 1989. Seismic velocities in mantle minerals and the mineralogy of the upper mantle. J. Geophys. Res. 94, 1895–1912.

Fuchs, K., Müller, G., 1971. Computation of synthetic seismograms with the reflectivity method and comparison with observations. Geophys. J. R. Astron. Soc. 23, 417–433.

Fukao, Y., Widiyantoro, S., Obayashi, M., 2001. Subductiong slabs stagnant in the mantle transition zone. Rev. Geophys. 39, 291–323.

Fukao, Y., Obayashi, M., Inoue, H., Nenbai, M., 1992. Subducting slabs stagnant in the mantle transition zone. J. Geophys. Res. 97, 4809–4822.

Grand, S.P., 2002. Mantle shear-wave tomography and the fate of subducted slabs. Phil. Trans. R. Soc. Lond. A 360, 2475–2491.

Grand, S.P., van der Hilst, R.D., Widiyantoro, S., 1997. Global seismic tomography: a snapshot of convection in the Earth. GSA Today 7 (4), 1–7.

Inoue, H., Fukao, Y., Tanabe, K., Ogata, Y., 1990. Whole mantle P wave travel time tomography. Phys. Earth Planet. Int. 59, 294–328.

Irifune, T., Higo, Y., Inoue, T., Kono, Y., Ohfuji, H., Funakoshi, K., 2008. Sound velocities of majorite garnet and the composition of the mantle transition zone. Nature 451, 814–817.

Irifune, T., Ringwood, A.E., 1987. Phase transformations in primitive MORB and pyrolite compositions to 25 GPa and some geophysical implications. In: Manghanani, M., Syono, Y. (Eds.), High Pressure Research in Geophysics, vol. 231. TERRAPUB/AGU, Washington, DC.

Irifune, T., Ringwood, A.E., 1993. Phase transformations in subducted oceanic crust and buoyancy relationships at depths of 600–800 km, in the mantle. Earth Planet. Sci. Lett. 117, 101–110.

Ita, J., Stixrude, L., 1992. Petrology, elasticity, and composition of the mantle transition zone. J. Geophys. Res. 97, 6849–6866.

Karato, S., Wang, Z., Liu, B., Fujino, K., 1995. Plastic deformation of garnets: systematics and implications for the rheology of the mantle transition zone. Earth Planet. Sci. Lett. 130, 13–30.

Katayama, I., Karato, S., 2008. The effect of water and iron content on the rheological contrast between garnet and olivine. Phys. Earth Planet. Int. 166, 57–66.

Kennett, B.L.N., Engdahl, E.R., 1991. Traveltimes for global earthquake location and phase identification. Geophys. J. Int. 105, 429–465.

Kono, Y., Higo, Y., Ohfuji, H., Inoue, T., Irifune, T., 2007. Elastic wave velocities of garnetite with a MORB composition up to 14 GPa. Geophys. Res. Lett. 34, L14308, doi:10.1029/2007GL030312.

Li, B., Rigden, S.M., Liebermann, R.C., 1996. Elasticity of stishovite at high pressure. Phys. Earth Planet. Int. 96, 113–127.

Nakagawa, T., Tajima, F., submitted for publication. Seismic broadband waveform modeling for a highly localized zone of low velocity anomaly associated with a stagnant slab. Geophys. Res. Lett.

Niu, F., Levander, A., Ham, S., Obayashi, M., 2005. Mapping the subducting Pacific slab beneath southwest Japan with Hi-net receiver functions. Earth Planet. Sci. Lett. 239, 9–17.

Ohtani, E., Litasov, K., Hosoya, T., Kubo, T., Kondo, T., 2004. Water transport into the deep mantle and formation of a hydrous transition zone. Phys. Earth Planet. Int. 143–144, 255–269.

Ringwood, A.E., 1967. The pyroxene-garnet transformation in the Earth's mantle. Earth Planet. Sci. Lett. 2, 255–263.

Ringwood, A.E., 1994. Role of the transition zone and 660 km discontinuity in mantle dynamics. Phys. Earth Planet. Int. 86, 5–24.

Ringwood, A.E., Irifune, T., 1988. Nature of the 650-km seismic discontinuity: implications for mantle dynamics and differentiation. Nature 331, 131–136.

Sano, A., Ohtani, E., Litasov, K., Kubo, T., Hosoya, T., Funakoshi, K., Kikegawa, T., 2006. In situ X-ray diffraction study of the effect of water on the garnet–perovskite transformation in MORB and implications for penetration of oceanic crust into the lower mantle. Phys. Earth Planet. Int. 159, 118–126.

Seno, T., Maruyama, S., 1984. Paleogeographic reconstruction and origin of the Philippine Sea. Tectonophysics 102, 53–84.

Shen, Y., Blum, J., 2003. Seismic evidence for accumulated oceanic crust above the 660-km discontinuity beneath southern Africa. Geophys. Res. Lett. 30, doi:10.1029/2003GL017991.

Sinogeikin, S.V., Bass, J.D., 2002. Elasticity of majorite and a majorite-pyrope solid 492 solution to high pressure: implications for the transition zone. Geophys. Res. Lett., 493 29: 1017.

Tajima, F., Fukao, Y., Obayashi, M., Sakurai, T., 1998. Evaluation of slab images in the northwestern Pacific. Earth Planets Space 50, 953–964.

Tajima, F., Grand, S.P., 1995. Evidence of high velocity anomalies in the transition zone associated with southern Kurile subduction zone. Geophys. Res. Lett. 22, 3139–3142.

Tajima, F., Grand, S.P., 1998. Variation of transition zone high velocity anomalies and depression of the 660 km discontinuity associated with subduction zones from the southern Kuriles to Izu-Bonin. J. Geophys. Res. 103, B7, 15015–15036.

Tajima, F., Nakagawa, T., 2006. Implications of seismic waveforms: complex physical properties associated with stagnant slab. Geophys. Res. Lett 33, L03311, doi:10.1029/2005GL024314.

Tajima, F., Nakakuki, T., Yoshioka, S., 2005. Seismological analysis and numerical simulations for mantle structure associated with stagnant slab. Zisin 2, 58, 121–141.

Turcotte, D.L., Schubert, G., 2002. Geodynamics, 2nd ed. Cambridge University Press, 456 pp.

van der Hilst, R.D., Engdahl, R., Sparkman, W., Nolet, G., 1991. Tomographic imaging of subducted lithosphere below northwest Pacific island arc. Nature 353, 37–43.

van der Hilst, R.D., Widiyantoro, S., Engdahl, E.R., 1997. Evidence for deep mantle circulation from global tomography. Nature 386, 578–584.

Wessel, P., Smith, W.H., 1995. New version of the Generic Mapping Tool released. EOS Trans. AGU 76, 329.

Widiyantoro, S., van der Hilst, R.D., 1996. Structure and evolution of lithospheric slab beneath the Sunda arc, Indonesia. Science 271, 1566–1570.

Xu, Y., Nishihara, Y., Karato, S., 2005. Development of a rotational Drickamer apparatus for large-strain deformation experiments at deep Earth conditions. In: Chen, J., et al. (Eds.), Advances in High-Pressure Techniques for Geophysical Applications. Elsevier, pp. 167–182.